Journal of Catalysis 260 (2008) 227–235

Contents lists available at ScienceDirect

Journal of Catalysis

www.elsevier.com/locate/jcat

How nitric oxide affects the decomposition of supported nickel nitrate to arrive at highly dispersed catalysts

Jelle R.A. Sietsma [1], Heiner Friedrich, Alfred Broersma, Marjan Versluijs-Helder, A. Jos van Dillen, Petra E. de Jongh, Krijn P. de Jong *

Inorganic Chemistry and Catalysis, Utrecht University, Sorbonnelaan 16, PO Box 80083, 3508 TB Utrecht, The Netherlands

ARTICLE INFO

Article history:
Received 31 March 2008
Revised 7 October 2008
Accepted 9 October 2008
Available online 28 October 2008

Keywords:
Catalysis
Calcination
Nitric oxide
Metal nitrates
Nickel
Hydrogenation
Catalyst preparation

ABSTRACT

An explanation is put forward for the beneficial effect of thermal decomposition of supported $Ni_3(NO_3)_2(OH)_4$ in NO/He flow (0.1–1 vol%) that enables preparation of well-dispersed (3–5 nm particles) 24 wt% Ni-catalysts via impregnation and drying using aqueous $[Ni(OH_2)_6](NO_3)_2$ precursor solution. Moreover, combining electron tomography, XRD and N_2-physisorption with SBA-15 support yielded a clear picture of the impact of air, He and NO/He gas atmospheres on NiO shape and distribution. TGA/MS indicated that NO_2, N_2O, H_2O products evolved more gradually in NO/He. *In situ* XRD and DSC revealed that NO lowers the nitrate decomposition rate and appears less endothermic than in air supposedly due to exothermic scavenging of oxygen by NO, which is supported by MS results. The Ni/SiO_2 catalyst prepared via the NO-method displayed a higher activity in the hydrogenation of soybean oil as the required hydrogenation time decreased by 30% compared to the traditionally air calcined catalyst.

1. Introduction

Supported metal (oxide) catalysts are indispensable for the preparation of bulk and fine chemicals [1–3]. Nickel-based catalysts are amongst the most widely used because of their activity in many important (de)hydrogenation reactions [4–7]. Since catalytic processes take place only at the metal (oxide) surface, preparation techniques often aim at obtaining catalysts that combine a high dispersion with a high loading. Although supported metal (oxide) particles can be obtained by deposition from the vapor phase [8], catalyst preparation techniques are mainly based on liquid phase processes and comprise of ion-adsorption [9,10], deposition–precipitation [11–13] and, impregnation and drying [14–18]. In particular the latter is often used as it enables high metal (oxide) loadings and its technical simplicity allows execution on an industrial scale. This technique involves impregnation of a support with a precursor-containing solution, followed by evaporation of the solvent. The dried impregnate is heat treated in air, called calcination, to convert the precursor into the desired metal oxide, optionally followed by a high temperature reduction treatment to obtain the metal in question. State-of-the-art studies at low Ni loadings and strong precursor–support interactions have revealed much insight into the interplay between metal, ligands, counterions and supports, and their impact on the activity, selectivity and stability of the final catalyst [13,16,17,19]. Moreover, these studies have yielded fundamental insight into the importance of liquid–solid interactions between precursor solution and support on the formation of poorly reducible mixed Ni phases like aluminates or phyllosilicates. However, at Ni loadings well-above the ion-adsorption capacity of the support and with a weak precursor–support interaction, phenomena like redistribution and sintering during the successive (thermal) steps in the preparation can prevail. In this contribution we present a systematic study that focussed on the preparation of Ni-based catalysts that display high loadings using the impregnation and drying method.

The type of precursor salt used largely affects the properties of the final metal (oxide). In particular highly soluble nitrate salts are attractive as pure metal oxides can be obtained via facile and complete thermal decomposition in air. Regrettably, catalysts prepared as such often display poor metal dispersions, which has been ascribed to either redistribution during drying [15,20–23] or to sintering during the air calcination [24–28] step. Using ordered mesoporous silica SBA-15 as model support, we recently reported for Ni and Co *ex* nitrate catalysts that this finds origin in severe sintering and redistribution during the air calcination treatment [29]. Moreover, we identified that sintering could be reduced using an He

* Corresponding author. Fax: +31302511027.
E-mail addresses: jelle.sietsma@shell.com (J.R.A. Sietsma), h.friedrich@uu.nl (H. Friedrich), a.broersma@uu.nl (A. Broersma), m.versluijs-helder@uu.nl (M. Versluijs-Helder), a.j.vandillen@uu.nl (A. Jos van Dillen), p.e.dejongh@uu.nl (P.E. de Jongh), k.p.dejong@uu.nl (K.P. de Jong).
[1] Current address: Shell Global Solutions International B.V., PO Box 38000, 1030 BN Amsterdam, The Netherlands.

0021-9517/$ – see front matter
doi:10.1016/j.jcat.2008.10.007

atmosphere, but that treatment in NO/He fully prevented sintering resulting in small NiO particles of 4 nm on average at a metal loading of 24 wt% [30,31]. Although the ordered structure of SBA-15 allowed clear differentiation between NiO and support with standard Transmission electron microscopy (TEM), the technique cannot give full insight into the NiO distribution throughout individual pores, as it yields a two-dimensional projection of the three-dimensional SBA-15 structure. This problem can be overcome using electron tomography (ET), sometimes referred to as 3D-TEM, as this technique allows three-dimensional imaging of the interior of porous structures such as SBA-15 [32–34]. Hence, ET could yield valuable insight into the impact of the air, He and NO/He atmospheres on the local distribution of NiO inside the mesopores and type of NiO particles formed. When combined with bulk-characterization techniques such as N_2-physisorption and XRD, a representative picture can be obtained.

In addition, it remained an open question why NO has such a large impact on the final NiO dispersion. Thus, we focused on the nitrate decomposition reaction under different atmospheres using TGA/MS, *in situ* XRD and DSC characterization techniques. Moreover, we varied the concentration of NO, and the gas flow rate. Based on these results we propose an explanation for the impact of NO on the nitrate decomposition to form uniform and small NiO nanoparticles. Finally, the large impact of the NO-method on the activity is illustrated with catalytic results of the hydrogenation of Soybean oil over silica gel supported 24 wt% Ni catalysts.

2. Experimental

2.1. Catalyst preparation

SBA-15 (total pore volume of 0.78 $cm^3\,g^{-1}$ and average pore diameter of 9 nm) was synthesized by following a procedure of Zhao and co-workers [35]. 8 g of $PEO_{20}PPO_{70}PEO_{20}$ (PEO = poly(ethylene oxide) and PO = poly(propylene oxide)) tri-block copolymer obtained from Aldrich was dissolved in 250 ml demineralized water of 40 °C. After the solution had become clear, 48 g of concentrated HCl (Merck) was added, followed by the addition of 21.5 ml of tetraethyl orthosilicate (Acros). Next, the mixture was stirred for 20 h at 40 °C after which it was transferred to an oven for further reaction at 80 °C for 48 h. The solid product was collected from the suspension by filtration, washing, drying in air for 12 h at 80 °C, and finally air calcination for 6 h at 550 °C. Davicat 1404SI silica gel (30–70 μm particles, total pore volume of 0.90 $cm^3\,g^{-1}$ and average pore diameter of 7 nm) was used as received from Grace–Davison.

The precursor solution was prepared by dissolving $Ni(NO_3)_2\cdot 6H_2O$ (Acros) in demineralized water. Prior to impregnation, the supports were dried for 2 h in dynamic vacuum at 80 °C to remove physisorbed water. SBA-15 and silica gel quantities of 0.25 g and 1.00 g were impregnated in static vacuum using 1.00 $ml\,g^{-1}$ and 1.25 $ml\,g^{-1}$ of precursor solution to provide 24 wt% and 28 wt% NiO/SiO_2, respectively. The fresh impregnates were dried in static air by increasing the temperature at a rate of 1 °C min^{-1} to 120 °C. The samples were kept at the final temperature for 12 h. Small quantities of 40 mg (SBA-15) and 100 mg (silica gel) of the dried impregnates were heat treated in an air, He or NO/He flow (90 $ml\,min^{-1}$) using a plug-flow reactor (length 17 cm and diameter 1 cm). The samples were heated with 1 °C min^{-1} to 450 °C kept at 450 °C for 4 h. The gas-hourly-space-velocities (GHSV) and NO concentrations were varied between 1700–24,500 h^{-1} and 0.01–1 vol%, respectively. Apparent bulk densities of 0.46 and 0.09 g cm^{-3} for silica gel and SBA-15, respectively, were used to calculate the GHSV. All samples were labeled using sample codes. An example of a sample code is S/D-C_{He}. The first part denotes the support: S = SBA-15 and G = silica gel support, whereas the second part indicates the thermal treatments that were applied: D = drying in static air, C_{He}= heat treatment in He flow.

2.2. Characterization

Powder X-ray diffraction (XRD) patterns were obtained at room temperature from 5 to 90° 2θ with a Bruker-AXS D8 Advance X-ray Diffractometer setup using Co$K_{\alpha 12}$ radiation. The patterns were baseline-corrected for the amorphous SiO_2 background. The average $Ni_3(NO_3)_2(OH)_4$ and NiO crystal sizes were calculated according to the Scherrer equation ($k = 1$) using the most intense (001) and (200) diffraction lines at $2\theta = 14.9°$ and 50.8°, respectively. For *in situ* XRD experiments the diffractometer was equipped with an Anton-Paar XRK reaction chamber and dried impregnate S/D (20 mg) was heated in air flow or in 1 vol% NO/He flow (90 $ml\,min^{-1}$) to 248 °C with 1 °C min^{-1} and kept isothermal until decomposition of $Ni_3(NO_3)_2(OH)_4$ and formation of NiO had completed.

TEM tomography grids were prepared by applying 10 nm sized colloidal gold particles from suspension to a Quantifoil R2/1 carbon film supported on a parallel bar Cu TEM grid. After drying in air, a small amount of sample was deposited directly onto the grid. Excess catalyst was shaken-off before inserting the TEM grid into a Fischione, Model 2020, advanced tomography holder. ET was performed in bright-field TEM mode, and series of TEM images (tilt-series) were acquired by rotating the specimen over a tilt range of at least ±70° at increments of 1°. Images were recorded at each tilt step on a 2048 pixel × 2048 pixel TVIPS CCD camera using Xplore3D software (FEI). The defocus was set between −130 nm and −200 nm depending on the size of the examined SBA-15 particle to keep the entire object in underfocus. The nominal magnification was 29000× which corresponds to a pixel size of 0.27 nm. Images of the tilt-series were aligned with respect to a common origin and rotation axis using the 10 nm gold particles as fiducial markers. Finally the aligned tilt-series were binned to 0.54 nm pixel size prior to reconstruction of the three-dimensional volume. Alignment and reconstruction by filtered backprojection was performed in IMOD [36].

N_2-physisorption measurements were performed at −196 °C, using a Micromeritics Tristar 3000 apparatus. Prior to analysis the samples were dried in He flow for 14 h at 120 °C. The pore size distribution was derived from the adsorption branch of the isotherm using a non-local density functional theory (NL-DFT) model developed by Jaroniec et al. [37] for ordered mesoporous supports. The pore diameter of the mesoporous channels of SBA-15 was defined by the value at which the maximum in differential pore volume was observed. The micro- and meso-porosity were defined as the volume present in pores smaller than 2 nm, and between 2 and 50 nm, respectively. There is no standard method yet for the determination of blocked mesopore volume ($V_{meso,bl}$). We used BJH theory [38] with the Harkins and Jura [39] thickness equation and the Kruk–Jaroniec–Sayari [40] correction for ordered mesoporous siliceous materials to calculate from the desorption branch the cumulative pore volume as a function of the pore size. From this we determined $V_{meso,bl}$ considering that the pores with a diameter of 2 to 5 nm are due to volume in (partially) blocked pores. The mesopore surface areas were calculated with the t-method using thickness ranges of 0.35–0.55 [41].

Thermogravimetric analysis (TGA) was carried out using a Perkin-Elmer Pyris 1 apparatus, a typical S/D sample quantity of 5 mg and air, He or 1 vol% NO/He flows of 90 $ml\,min^{-1}$. A heating rate of 5 °C min^{-1} and final temperature of 500 °C was used. The off-gas was simultaneously analyzed with a quadrupole Pfeiffer Omnistar mass spectrometer, and ion currents were recorded for m/z values (m = molar mass of X^{z+} ion, z = charge of the ion) of 14, 15, 16, 17, 18, 28, 30, 32, 44, 46, 62 and 63.

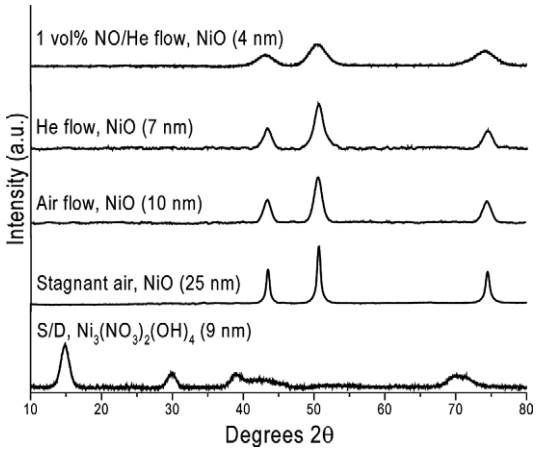

Fig. 1. XRD patterns of SBA-15 supported impregnate S/D after drying at 120 °C, and NiO/SBA-15 samples obtained thereof after thermal treatment at 450 °C using different gas atmospheres. The resulting average crystal sizes and gas atmospheres have been indicated.

Differential scanning calorimetry (DSC) experiments were done using a Q200 Thermal Analysis Instruments apparatus. Small quantities (~5 mg) of sample S/D were heated to 300 °C with 1 °C min^{-1} under a 90 ml min^{-1} flow of either air, Ar or 1 vol% NO/He.

2.3. Catalysis

Hydrogenation reactions of soybean oil with an iodine value (IV) of 133 were carried out using 28 wt% NiO on silica gel catalysts obtained after air calcination (G/D-C_{air}) or NO/He treatment (G/D-$C_{NO/He}$). A portion of 70 mg of NiO/SiO_2 sample was weighed into a glass vessel and reduced for 1 h at 400 to 450 °C under atmospheric H_2 pressure. The reduced catalyst was transferred into 200 g of soybean oil and loaded to a closed and stirred hydrogenation reactor (Medimex). The mixture was heated to 140 °C and H_2 sparged through the slurry at a pressure of 3 bar abs. The temperature was raised by 2 °C min^{-1} to 200 °C and kept at that temperature. The amount of H_2 absorbed into the oil was monitored with a Büchi gas dosage unit and the test was terminated once the IV had dropped to 79. The hydrogenation time to reach an IV of 79 was used as a measure of the activity of the catalyst. The melting point and percentage of trans-isomers were determined using standard methods [42,43].

3. Results and discussion

Fig. 1 shows the XRD pattern of the dried impregnate S/D obtained after impregnation of SBA-15 with aqueous $[Ni(OH_2)_6](NO_3)_2$ solution and subsequent drying at 120 °C. The results of XRD line-broadening analysis obtained for all the samples have been summarized in Table 1 together with TEM particle size estimations. The diffractogram of sample S/D showed that nickel nitrate hydroxide, also referred to as basic nickel nitrate, with composition $Ni_3(NO_3)_2(OH)_4$ had formed [44,45]. Line-broadening analysis of the (001) diffraction line indicated that the crystallites were 9 nm on average, which agreed well with the average mesopore diameter of 9 nm as determined from N_2-physisorption, and suggested confinement by the pore walls.

The second step in the preparation involved heat treatment of the dried impregnate at 450 °C to convert $Ni_3(NO_3)_2(OH)_4$ into NiO:

$$Ni_3(NO_3)_2(OH)_4(s) \rightarrow 3NiO(s) + 2NO_2(g) + \frac{1}{2}O_2(g) + 2H_2O(g). \quad (1)$$

Table 1
Overview sample treatments, compositions and XRD and STEM results.

	Thermal treatments	Crystalline phase	Loading (wt%)	Size (nm)	
				d_{XRD}	d_{STEM}
SBA-15 supported samples					
S/D	Drying	$Ni_3(NO_3)_2(OH)_4$	34	9	–
S/D-C_{air}	Drying/calcination in air	NiO	24	10	10–35
S/D-C_{He}	Drying/heating in He	NiO	24	7	10–25
S/D-$C_{NO/He}$	Drying/heating in 1 vol% NO/He	NiO	24	4	3–5
Silica gel supported samples					
G/D	drying	$Ni_3(NO_3)_2(OH)_4$	39	12	–
G/D-C_{air}	Drying/calcination in air	NiO	28	15	7–70
G/D-$C_{NO/He}$	Drying/heating in 1 vol% NO/He	NiO	28	4	3–5

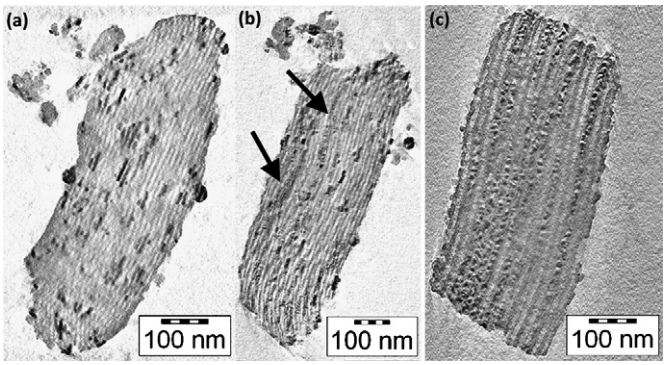

Fig. 2. ET slices of NiO/SBA-15 samples obtained after calcination in air flow (a), thermal treatment in He flow (b), and heat treatment in 1 vol% NO/He flow (c). The arrows indicate regions containing small NiO particles.

In Fig. 1, the XRD patterns are shown of the NiO/SBA-15 products obtained using different gas atmospheres during this step. It should be noted that the same flow rates were used in all the plug–flow experiments unless otherwise stated. Line-broadening analysis showed that thermal decomposition in stagnant air resulted in relatively large NiO crystals of 25 nm on average, use of an air flow led to crystals of 10 nm and with a pure He flow an average crystallite size of 7 nm was obtained. Adding 1 vol% of NO to the He flow resulted in the formation of NiO crystallites of 4 nm on average. The observed differences showed the impact of the gas atmosphere on the degree of sintering and redistribution during thermal decomposition of $Ni_3(NO_3)_2(OH)_4$.

In Fig. 2, three representative 0.54 nm thick cross-sections through the ET reconstructions are given of the NiO/SBA-15 samples that were treated in air (sample S/D-C_{air}), pure He (S/D-C_{He}) or 1 vol% NO/He (S/D-$C_{NO/He}$). A non-uniform distribution of NiO over the mesopores was found in all three samples. The presence of unfilled pores with ordered mesoporous silica supported metal (oxide) catalysts has been observed by others too [46,47] and is presumably related to non-uniform wetting during impregnation [48]. The NiO/SBA-15 sample obtained through air calcination contained both large NiO particles outside the mesopores and particles retained inside the pores. The ET reconstruction showed that all the NiO particles inside the mesopores were rod-like with a diameter of 9 nm due to confinement by the pore walls, and their length varied between 10 to 70 nm with an average value of 35 nm. No special location of the NiO particles, for instance at the pore mouths of the mesopores, was observed. After thermal treatment in He (Fig. 2b) three types of NiO particles could be identified; large particles outside the mesopores and, rodlike and more spherical particles inside the mesopores. Again, the rodlike NiO particles were confined by the pore walls, but their length had decreased to 10–40 nm and 20 nm on average. Areas containing smaller and more spherical NiO particles were found too, as

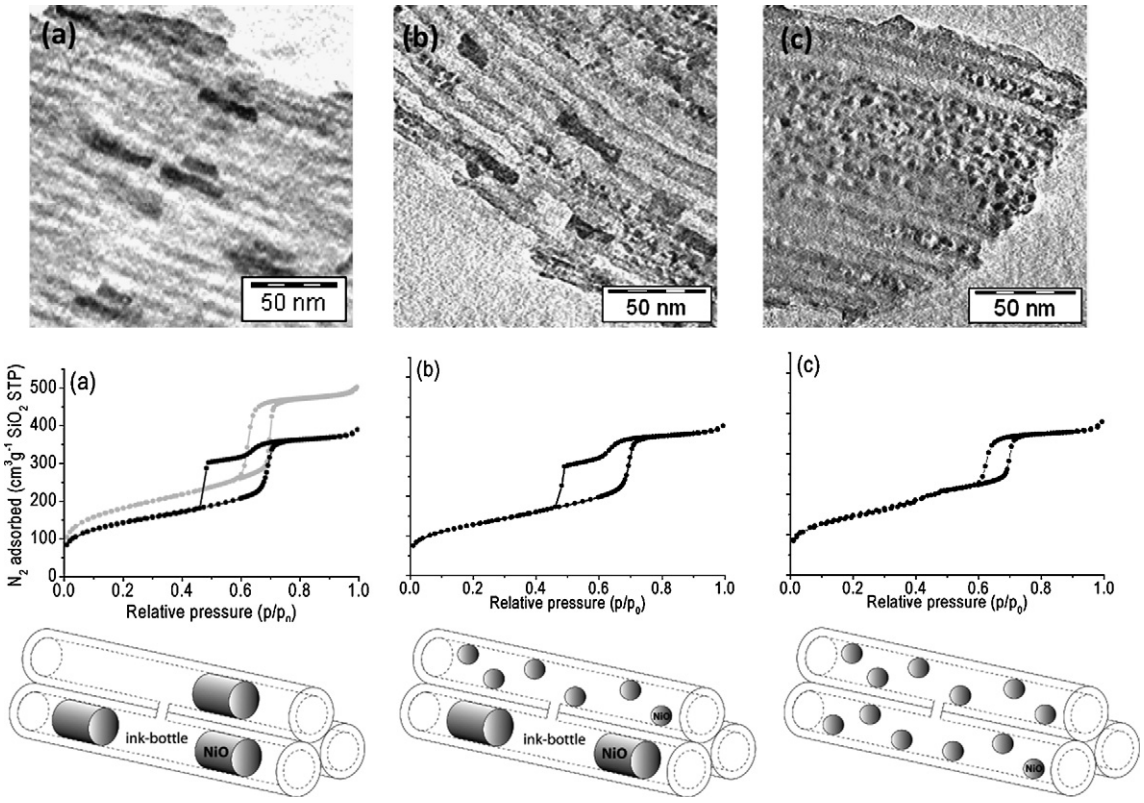

Fig. 3. ET slices, N_2-physisorption isotherms and schematic representations of the NiO particle distribution inside the mesopores and of NiO/SBA-15 samples obtained after heating to 450 °C of dried impregnate S/D in air flow (a), in pure He flow (b) or in 1 vol% NO/He flow (c). Also included is the isotherm of pristine SBA-15 (grey).

Table 2
N_2-physisorption results of SBA-15 supported samples.

Sample	Surface area[a] ($m^2\ g_{SiO_2}^{-1}$)	Porosity ($cm^3\ g_{SiO_2}^{-1}$)				$V_{meso,bl}$[f] (%)
		$V_{tot,calc}$[b]	$V_{tot,exp}$[c]	V_{micro}[d]	V_{meso}[e]	
SBA-15	516	0.78	0.78	0.05	0.68	0
S/D	293	0.63	0.47	0.01	0.42	19
S/D-C_{air}	409	0.73	0.66	0.06	0.56	74
S/D-C_{He}	442	0.73	0.59	0.03	0.51	57
S/D-$C_{NO/He}$	493	0.73	0.59	0.05	0.49	0

[a] Mesopore surface area.
[b] Expected total pore volume based on contribution of Ni precursor to volume decrease.
[c] Total pore volume based on amount N_2 adsorbed at $p/p_0 = 0.995$.
[d] Micropore volume.
[e] Mesopore volume.
[f] Partially blocked mesopore volume.

indicated by the arrows in Fig. 2b. XRD (Fig. 1) supported the ET findings as the onset of the diffraction lines had broadened indicating a bimodal particle size distribution. Finally, Fig. 2c depicts a slice taken from a three-dimensional reconstruction of a NiO/SBA-15 particle prepared with NO/He. Exclusively small NiO particles were found in this sample and although particles between 2 to 7 nm were found, detailed particle-size analysis published elsewhere [49] showed that 80% of the particles were 3 to 5 nm. Moreover, a volume weighted NiO size maximum of 4 nm was found, which was in good agreement with the average crystal size of 4 nm derived from the XRD pattern shown in Fig. 1.

Combination of the ET results with characterization results from N_2-physisorption and XRD (Table 2) allowed us to put together representative pictures of the NiO particle distributions inside the mesopores of the air, He and NO/He treated samples. In Fig. 3, ET slices and N_2-physisorption results of the samples are shown together with schematic illustrations that represent the NiO distribution inside the pores as a function of the gas atmosphere. With ET (Fig. 3a) we found in the air treated sample many voids between the rodlike NiO particles situated in the same pore. A movie that images such a void has been included in the supporting information (void.mpg). Compared to the pristine SBA-15 that contained all features typical for SBA-15 [35], the air calcined sample displayed a forced closure of the hysteresis loop. This feature is referred to as cavitation and associated with ink-bottle type pores [50]. The appearance of cavitation upon introduction of a guest phase [33,51] or plugs [52] to SBA-15 has been previously reported. Quantification (Table 2) showed that 74% of the mesopore volume ($V_{meso,bl}$) was blocked by the rodlike NiO particles. In He atmosphere (Fig. 3b), similar ink-bottles were found with ET, hence cavitation was also observed in the isotherm. However, quantification showed that the total blocked mesopore volume had lowered to 57%. As schematically illustrated in Fig. 3, this was in line with the observation that pores with smaller NiO particles, that allowed normal hysteresis, were present too. Finally, in NO/He (Fig. 3c) the well-dispersed NiO particles were small enough (3 to 5 nm), had not agglomerated and hence the sample displayed hysteresis similar to that of pristine SBA-15. The observed trend in the mesopore volumes supported the abovementioned findings as the porosity decreased going from air to He, and to NO/He due to the more extensive retention of the NiO guest phase inside the mesopores for the latter cases. Thus, with ET analysis we could directly image the NiO distribution inside individual mesopores, and combined with N_2-physisorption and XRD bulk characterization this led to a consistent insight into the influence of the gas atmosphere on the obtained NiO particle distribution inside the mesopores of SBA-15.

The experiments with stagnant air and with air flow (see Fig. 1) demonstrated that the concentration of gaseous decomposition products had a profound impact on the final NiO dispersion. Hence, insight into the interplay between NO and these products, and its effect on the NiO dispersion was important to better understand the role of NO. Therefore, we conducted a series of ex-

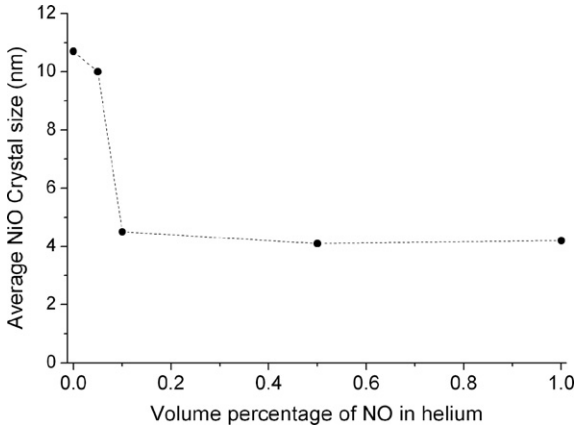

Fig. 4. Impact of the NO concentration on the final average NiO crystal size obtained after heat treatment of silica gel supported $Ni_3(NO_3)_2(OH)_4$ sample G/D. A constant GHSV of 24,500 h^{-1} was used.

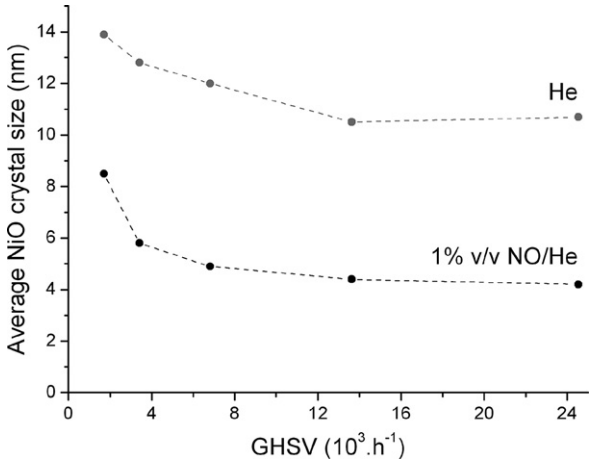

Fig. 5. Relation between the GHSV and the average NiO crystal size obtained during thermal treatment of $Ni_3(NO_3)_2(OH)_4/SiO_2$ sample G/D in He (grey) or in NO/He (black).

periments in which on the one hand the NO concentration was varied while maintaining a constant flow rate (i.e. constant GHSV), and on the other hand the GHSV was varied at constant NO/He concentration (1 vol%). To ensure plug–flow conditions we used a conventional silica gel powder sieve fraction instead of the low-density SBA-15. Silica gel powder with a porosity (0.90 $cm^3\,g^{-1}$) and an average pore size (7 nm) comparable to that of the SBA-15 was selected. Prior to the plug–flow experiments, it was checked whether the impact on the NiO dispersion found with silica gel was similar as with SBA-15. From the results collected in Table 1 it can be concluded that indeed the same trends were found. In Fig. 4, the relation has been plotted between the NO/He concentration and the average NiO crystal size obtained as determined with XRD. Without addition of NO to the He flow an average NiO crystal size of almost 11 nm was obtained. Adding a small amount of 0.05 vol% NO only had a small impact, but doubling to 0.1 vol% led to a decrease by more than a factor of two of the average crystal size. Further increase of the concentration had little effect as the average NiO crystal size of 4 nm remained constant. Thus, at the present loading of 28 wt% NiO and high GHSV of 24,500 h^{-1}, a concentration of 0.1 vol% NO/He was sufficient to obtain small NiO crystallites of 4 nm on average.

The results obtained when varying the GHSV between 1700 to 24,500 h^{-1} with pure He flow or NO/He flow (1 vol%) are shown in Fig. 5. The results demonstrated that the obtained average NiO crystal sizes with NO/He were always smaller than with pure He.

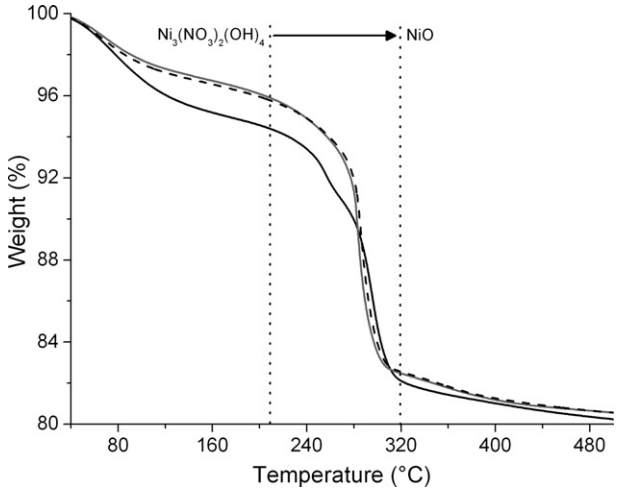

Fig. 6. TGA curves recorded during thermal treatment of sample S/D in air flow (dashed line), Ar flow (grey line) or in 1 vol% NO/He flow (black line).

With the latter gas atmosphere, the average NiO crystal size started to increase at a GHSV lower than ~14,000 h^{-1}. Although decreasing the GHSV with a factor of 2 had little effect, further lowering led to more sintering and finally an average crystal size of almost 14 nm was found. Although at all times smaller NiO crystals were obtained with NO/He, the crystal sizes followed a similar trend as with pure He. Lowering of the GHSV by more than a factor of 7 from 24,500 to 3400 h^{-1} led to a rise of the crystal size of around 4 nm to that of 6 nm. Further decrease of the GHSV resulted in substantial rise of the average NiO crystal size to 9 nm, but still being smaller than with pure He. These results suggest the relation between the NiO crystal size and the concentration of gaseous decomposition products, and the necessity of a minimum local NO concentration to moderate the $Ni_3(NO_3)_2(OH)_4$ decomposition in such as way that small NiO particles are formed.

To identify the type of gaseous decomposition products formed, we conducted TGA/MS experiments using SBA-15 supported impregnate S/D. The results obtained with 1 vol% NO/He flow were compared with those obtained in air flow and in pure Ar flow. The TGA and MS results are shown in Figs. 6 and 7, respectively. For all samples up to ~200 °C removal of physisorbed H_2O and partial dehydroxylation of the SiO_2 surface took place. Evolved gas analysis results supported this as only mass fractions were detected that belonged to H_2O. Surprisingly, at 210 °C weight loss due to dehydration of the NO/He flow treated sample was almost 1.5% larger than those treated in air or in Ar flow. At higher temperatures, irrespective of the atmosphere used, the weight losses rapidly increased till a temperature of ~320 °C was reached. The observed weight losses for air (13%), Ar (13%), and NO/He (12.5%) atmosphere matched or were close to the expected value of 13% upon complete decomposition of $Ni_3(NO_3)_2(OH)_4$ into NiO. MS results showed that H_2O, NO_2 and O_2 gaseous products were formed as expected based on Eq. (1). The MS signal with $m/z = 18$ originated from H_2O and was found in all atmospheres. Mass fraction 17 (OH^+) was found to support the assignment to H_2O. Mass fraction 46 confirmed that significant amounts of NO_2 formed during decomposition, irrespective of the atmosphere. In Ar flow we detected, albeit in relatively small amounts, $m/z = 32$ indicative for O_2. Next to these expected products also mass fraction 44 was found to evolve during each treatment, and this indicated that either N_2O, CO_2 or a mixture of these compounds was formed. With GC analysis we could confirm that this mass fraction originated exclusively from N_2O, which is in line with observations of Małecki et al. [53] that 5 to 8 wt% of the nitrogen from nitrates evolves as N_2O. A remarkable difference was that O_2 was not

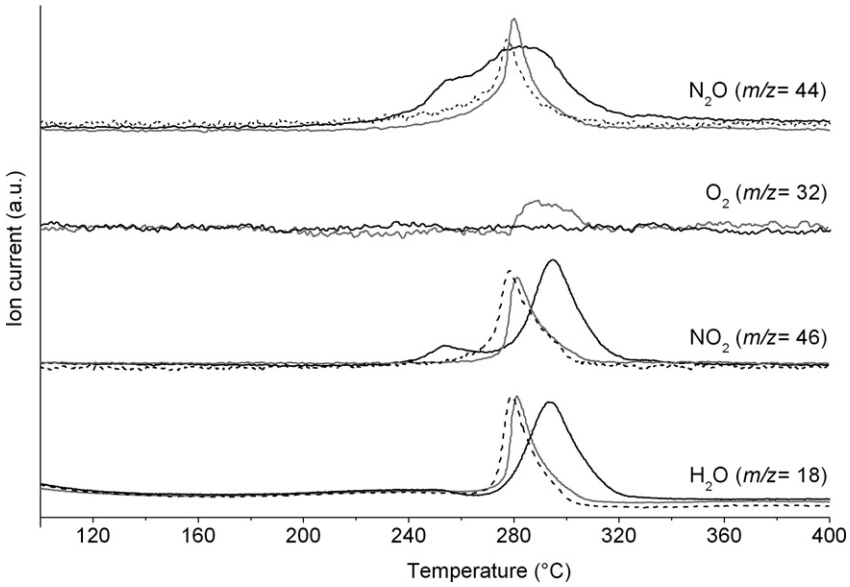

Fig. 7. MS results obtained from the off-gas during thermal treatment of $Ni_3(NO_3)_2(OH)_4/SiO_2$ sample S/D in air flow (dashed lines), in pure Ar flow (grey lines) or in 1 vol% NO/He (black lines).

found during decomposition in NO/He. Furthermore, in NO/He the bulk of the gasses evolved over a broader temperature range and, apart from N_2O, the peaks also shifted to higher temperatures. This indicated that NO influenced the kinetics of the $Ni_3(NO_3)_2(OH)_4$ decomposition, and the absence of O_2 during decomposition in NO/He suggested that NO might scavenge atomic oxygen that is expected to play a role in the mechanism of the decomposition of $Ni_3(NO_3)_2(OH)_4$.

As the TGA/MS results indicated that NO affected the rate of decomposition of $Ni_3(NO_3)_2(OH)_4$ into NiO, and both phases were crystalline, we carried out *in situ* XRD experiments to study the possible moderation of the reaction rate by NO in more detail. The most intense (001) and (002) diffraction lines of $Ni_3(NO_3)_2(OH)_4$ and NiO at 14.9° and 50.8° 2θ (see Fig. 1) were used for this, respectively. The experiments were carried out with sample S/D and consisted of heating to 248 °C and maintaining isothermal conditions during decomposition as this could give more insight into the kinetics. The observed $Ni_3(NO_3)_2(OH)_4$ decomposition and NiO formation at 248 °C in air flow or in 1 vol% NO/He flow have been plotted in Fig. 8. The left frame graph showed that after an incubation time of almost 25 min, decomposition proceeded relatively fast in air at a rate of $\sim$13% min^{-1}, and about 85% of the $Ni_3(NO_3)_2(OH)_4$ decomposed within 6.5 minutes. In NO/He atmosphere, decomposition started almost immediately and though the initial rate was somewhat higher (3.6% min^{-1}), a relatively low constant rate of 2.7% min^{-1} throughout the entire process was observed. As a result decomposition of the $Ni_3(NO_3)_2(OH)_4$ proceeded gradually over 34 min and took longer than in air. Moreover, a remarkable difference between the decomposition profiles in air and NO/He was observed. The former displayed an 'autocatalytic' type of trend, whereas the latter suggested zero-order kinetics. Finally, the plot on the right-hand side of Fig. 8 demonstrated for both gas atmospheres that decomposition of $Ni_3(NO_3)_2(OH)_4$ was accompanied by formation of NiO without delay. In other words, the NiO formation followed an inverse profile, suggesting that no intermediate phases were formed. Similar *in situ* experiments that consisted of heating to 450 °C at a rate of 1 °C min^{-1} qualitatively supported the findings obtained at isothermal heating at 248 °C, but the decomposition rates had increased to 15.8% min^{-1} for air and to 6.6% min^{-1} for NO/He. Moreover, these *in situ* results showed that the average NiO crystal size observed after thermal decomposition had completed was not affected by further heating to 450 °C, and we concluded that in air precursor migration took place only during the decomposition of $Ni_3(NO_3)_2(OH)_4$ into NiO. Use of an NO/He flow clearly moderated the kinetics of the $Ni_3(NO_3)_2(OH)_4$ decomposition and with the average decomposition rate we could roughly estimate the rate at

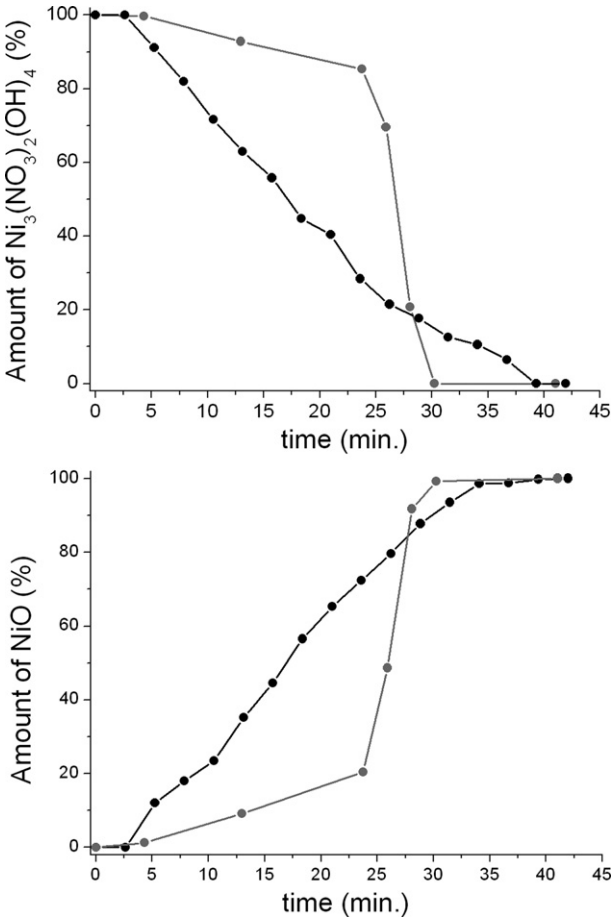

Fig. 8. *In situ* XRD results obtained during thermal decomposition of $Ni_3(NO_3)_2(OH)_4$/SBA-15 sample S/D into NiO at a constant temperature of 248 °C either under air flow (grey lines) or under 1 vol% NO/He flow (black lines).

which NO_2, H_2O and oxygen evolved. Since reaction of NO with NO_2 or H_2O was unlikely, we compared the amount of oxygen evolved with that of the 1 vol% of NO added during the reaction. Using the decomposition rate of 6.6% min^{-1} a NO:O_2 ratio of 32 was calculated, which indicated that the amount of NO sufficed to react with all the oxygen formed during decomposition.

Thus far, the results showed on the one hand that NO moderated the decomposition rate of $Ni_3(NO_3)_2(OH)_4$, and indicated on the other hand that NO suppressed the formation of O_2. As both these processes would induce heat flow differences we recorded DSC traces during heat treatment of sample S/D in air flow or in 1 vol% NO/He flow. The results are given in Fig. 9. Firstly, both heat flow curves showed to be endothermic, as expected, and similar to the decomposition of $Ni(NO_3)_2{\cdot}6H_2O$ [54,55]. Secondly, the trace recorded during decomposition in air had a very sharp peak with a maximum at 268 °C, whereas the NO/He trace consisted of a broad peak from 250 to 277 °C. Hence, the DSC results confirmed that NO moderated the decomposition rate of $Ni_3(NO_3)_2(OH)_4$. In air flow a heat of reaction of +241 $J\,g^{-1}$ $Ni_3(NO_3)_2(OH)_4$ was found while during NO/He treatment a heat of reaction of +202 $J\,g^{-1}$ $Ni_3(NO_3)_2(OH)_4$ was observed. These differences suggested that NO played a role in lowering the heat of reaction of $Ni_3(NO_3)_2(OH)_4$ into NiO.

Although the enthalpy of formation of $Ni_3(NO_3)_2(OH)_4$ is not exactly known, an indication for the reaction enthalpies could be obtained using the heat of formation of $Ni(NO_3)_2$ [56]. The endothermic decomposition of $Ni(NO_3)_2$ is usually accompanied by the formation of molecular oxygen:

$$Ni(NO_3)_2(s) \rightarrow NiO(s) + 2NO_2(g) + \frac{1}{2}O_2(g),$$
$$\Delta H_r^0 = +241\ \text{kJ mol}^{-1}. \quad (2)$$

Although the exact mechanism of this reaction (2) is not known to us, we propose that the formation of O_2 is the rate determining step. In fact O_2 has to be formed from two oxygen radicals emerging from two nitrate groups. The combination of two radicals to form O_2 is most likely a surface catalyzed process and NiO amongst other transition metal oxides such as MnO_2, Fe_2O_3 and CuO have been reported [57–60] to display relatively high activities in this reaction:

$$2O \rightarrow O_2(g). \quad (3)$$

If NiO indeed catalyzed reaction (3) it would explain the autocatalytic behavior of the decomposition in air (Fig. 8). The role of NO can now be understood as follows. First, the overall reaction in the presence of NO excludes formation of O_2 (cf. Fig. 7) and reads as follows:

$$Ni(NO_3)_2(s) + NO \rightarrow NiO(s) + 3NO_2(g),$$
$$\Delta H_r^0 = +184\ \text{kJ mol}^{-1}. \quad (4)$$

The lowering of the ΔH_r^0 from 241 to 184 $kJ\,mol^{-1}$ is in line with the DSC results. Second, NO affects the equilibria of reactions (2) and (4). In Fig. 10, the temperature dependency of the thermodynamic equilibria of Eqs. (2) (top-frame) and (4) (bottom-frame) have been plotted. The plots add to the proposed explanation of the impact that NO might have on the decomposition of $Ni_3(NO_3)_2(OH)_4$. With NO present, decomposition of $Ni(NO_3)_2$ becomes thermodynamically feasible at lower temperatures than without NO. Hence, this might explain the DSC findings (Fig. 9) that the decomposition in NO started earlier than in air. Moreover, the graphs show that formation of O_2 during decomposition is only thermodynamically favorable if NO is not present, which is in line with the MS results obtained for thermal decomposition of $Ni_3(NO_3)_2(OH)_4$ in NO/He and Ar (Fig. 7). It has already

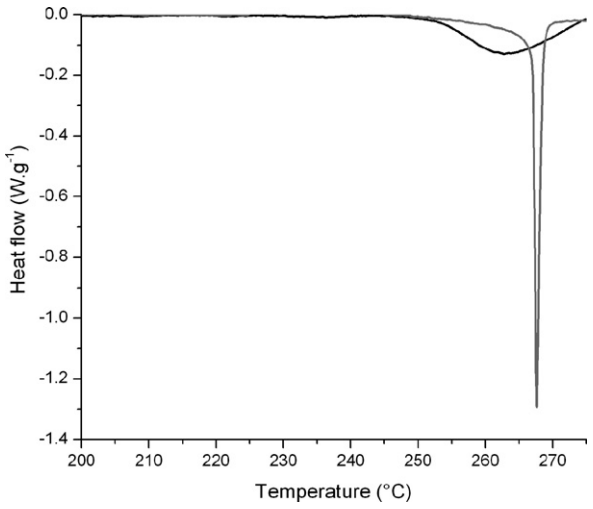

Fig. 9. DSC heat flow traces obtained during heating at 1 °C min^{-1} ramp of SBA-15 supported $Ni_3(NO_3)_2(OH)_4$ sample S/D under air flow (grey line) or under 1 vol% NO/He flow (black line).

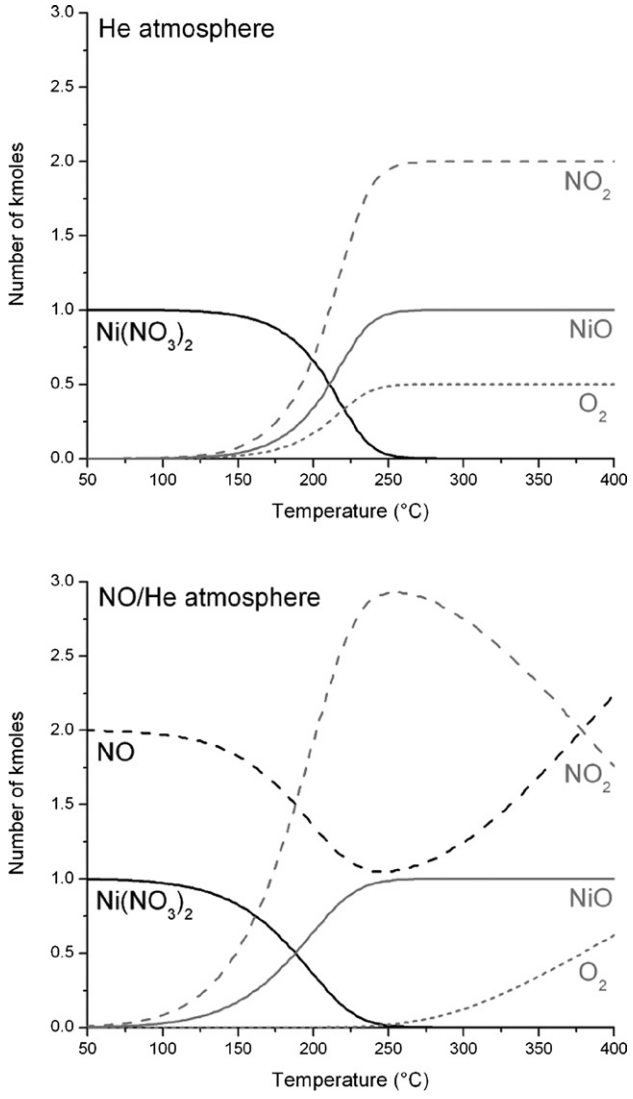

Fig. 10. Calculated plots [56] of the temperature dependency of the thermodynamic equilibria (1 bar) of $Ni(NO_3)_2$ with NiO and gaseous NO_2 and O_2 without (top-frame) or with NO (bottom-frame). Input: 1 kmol $Ni(NO_3)_2$, 10 kmol He, 2 kmol NO (NO/He).

Table 3
Soybean hydrogenation results of silica gel supported Ni catalysts.

Catalyst	Hydrogenation time (min)	End IV (gI_2/100 g)	Trans (%)	Melting point (°C)
G/D-C_{air}	148	79.0	34.8	45.4
G/D-$C_{NO/He}$	101	79.2	37.7	45.0

been demonstrated that H_2 has a beneficial impact on the dispersion of supported metal (oxide) particles too [48,61]. Moreover, we recently discovered that N_2O also has an advantageous effect [62]. Therefore, we propose that the presence of oxygen scavenging compounds such as NO, N_2O, CO and H_2 is crucial for preventing sintering and redistribution during thermal decomposition of supported transition metal (Fe, Co, Ni, and Cu) nitrates into their respective oxides.

Finally, the relevance of the NO-method for catalysis was studied by comparing the activities in the hydrogenation of soybean oil of reduced silica gel supported NiO catalysts with a Ni metal loading of 24 wt% prepared either through calcination in air flow (G/D-C_{air}) or heat treatment in 1 vol% NO/He flow (G/D-$C_{NO/He}$). The iodine value (IV) is a measure for the number of unsaturated double bonds present in oil and hence we used the time needed by the catalyst to decrease the IV from 133 to 79 $gI_2 \cdot 100\ g^{-1}$ as a measure of its activity.

The hydrogenation results are given in Table 3 and the percentage of trans-isomers and melting points of the fats turned out to be almost identical and had not been affected by the preparation method. The hydrogenation times showed that preparation of Ni/SiO_2 catalysts via the NO treatment instead of using traditional air calcination led to a reduction of ~30% in required hydrogenation time, which was relatively modest given the large nickel dispersion differences. Based on literature we conclude that the monomodal pore system of our catalyst with pores around 7 nm will lead to severe diffusion limitation for the soybean hydrogenation. This limitation likely masked the intrinsic differences in catalytic activity between the air calcined and NO treated catalysts G/D-C_{air} and G/D-$C_{NO/He}$ [63,64]. This explains that the improvement of catalytic activity going form air to NO calcination appeared more modest than previously observed for CO hydrogenation [31].

We conclude that the NO-method demonstrated to be a facile and effective way to improve the performance of catalysts prepared using nitrate precursors.

4. Conclusions

The impact of air, He and NO/He gas atmospheres on the thermal decomposition of supported $Ni_3(NO_3)_2(OH)_4$ was studied. By combining ET, N_2-physisorption and XRD a consistent picture of the distribution and sizes of NiO particles inside the mesopores of SBA-15 as a function of the gas atmosphere was obtained. ET results confirmed that after treatment in air exclusively rodlike NiO particles (9×35 nm) confined by the pore walls were present inside the mesopores. During heat treatment in pure He predominantly rodlike NiO particles (9×20 nm) were formed inside the mesopores as well, but also pores were identified that contained smaller more spherical particles.

Experiments with conventional silica gel showed that at all GHSV values smaller crystals could be obtained with NO, and with a GHSV of 24,500 h^{-1}, 0.1 vol% NO/He was already sufficient to obtain small 4 nm particles at a loading of 28 wt% NiO.

TGA/MS results showed that the NO_2, N_2O, H_2O gaseous decomposition products evolved more gradually in NO/He than in air or in pure He, and *in situ* XRD and DSC experiments confirmed that NO moderated the decomposition rate of $Ni_3(NO_3)_2(OH)_4$ into NiO, and proceeded much slower than in air. The heat of reactions as determined with DSC suggested that decomposition in NO/He was less endothermic than in air, which might be explained by the exothermic scavenging of oxygen radicals by NO. MS results are in line this hypothesis as no O_2 was detected amongst the gaseous decomposition products in NO/He flow contrary to treatment in pure Ar flow. Based on these results and prior findings we conclude that the presence of oxygen scavenging radicals such as NO, H_2, N_2O and CO is a prerequisite to prevent sintering and redistribution during nitrate decomposition.

The NO-treatment yielded, after high-temperature reduction, a Ni/SiO_2 catalyst that displayed a 30% higher activity compared to the catalyst treated through standard air calcination. The NO-treatment yielded, after high-temperature reduction, a Ni/SiO_2 catalyst that displayed a 30% higher activity compared to the catalyst treated through standard air calcination. This modest activity improvement was most likely related to diffusion limitation of our catalysts for the soybean hydrogenation.

The thermal decomposition of supported metal nitrates in a NO/He flow showed to be a versatile and robust method to obtain highly dispersed metal oxide particles and more active metal catalysts when followed by high-temperature reduction, and is a promising technique for the preparation of a wide range of well-dispersed metal (oxide) catalysts through impregnation and drying of nitrate precursor solutions.

Acknowledgments

Rudolf Mollema and Els Verdonck from TA Instruments and, Herre Talsma and Mies van Steenbergen from the department of pharmaceutics are kindly thanked for their help with DSC analysis. Martin Lok and Bart Zwijnenburg are acknowledged for hydrogenation experiments and discussions.

Supporting information

The online version of this article contains additional supporting information.

Please visit DOI: 10.1016/j.jcat.2008.10.007.

References

[1] A.T. Bell, Science 299 (2003) 1688–1691.
[2] R. Schögl, S.B. Abd Hamid, Angew. Chem. Int. Ed. 43 (2004) 1628–1637.
[3] J.Y. Ying, Chem. Eng. Sci. 61 (2006) 1540–1548.
[4] M.W. Balakos, E.E. Hernandez, Catal. Today 35 (1997) 415–425.
[5] P. Fouilloux, Appl. Catal. 8 (1983) 1–42.
[6] R.R. Allen, J. Am. Oil Chem. Soc. 63 (1986) 1328–1332.
[7] P. Fouilloux, Appl. Catal. 8 (1983) 1–42.
[8] P. Serp, P. Kalck, R. Feurer, Chem. Rev. 102 (2002) 3085–3128.
[9] M. Schreier, J.R. Regalbuto, J. Catal. 225 (2004) 190–202.
[10] X. Carrier, J.F. Lambert, M. Che, J. Am. Chem. Soc. 119 (1997) 10137–10146.
[11] L.A.M. Hermans, J.W. Geus, Stud. Surf. Sci. Catal. 3 (1979) 113–130.
[12] M.K. Van der Lee, A.J. Van Dillen, J.H. Bitter, K.P. De Jong, J. Am. Chem. Soc. 127 (2005) 13573–13582.
[13] M. Che, Z.X. Cheng, C. Louis, J. Am. Chem. Soc. 117 (1995) 2008–2018.
[14] K. Bourikas, C. Kordulis, A. Lycourghiotis, Catal. Rev. 48 (2006) 363–444.
[15] A.J. Van Dillen, R.J.A.M. Terörde, D.J. Lensveld, J.W. Geus, K.P. De Jong, J. Catal. 216 (2003) 257–264.
[16] O. Clause, M. Kermarec, L. Bonnevoit, F. Villain, M. Che, J. Am. Chem. Soc. 114 (1992) 4709–4717.
[17] J.Y. Carriat, M. Che, M. Kermarec, M. Verdaguer, A. Michalowicz, J. Am. Chem. Soc. 120 (1998) 2059–2070.
[18] A. Lekhal, B.J. Glasser, J.G. Khinast, Chem. Eng. Sci. 59 (2004) 1063–1077.
[19] F. Négrier, E. Marceau, M. Che, J.-M. Giraudon, G. Gengembre, A. Löfberg, J. Phys. Chem. B 109 (2005) 2836–2845.
[20] M. Kotter, L. Riekert, Stud. Surf. Sci. Catal. 2 (1979) 53–63.
[21] D.J. Lensveld, J.G. Mesu, A.J. Van Dillen, K.P. De Jong, Microporous Mesoporous Mater. 44–45 (2001) 401–407.
[22] K. Fang, J. Ren, Y. Sun, Mol. Catal. A Chem. 229 (2005) 51–58.
[23] P.J. Van den Brink, A. Scholten, A. Van Wageningen, M.D.A. Lamers, A.J. Van Dillen, J.W. Geus, Stud. Surf. Sci. Catal. 63 (1991) 527.
[24] B. Vos, E.K. Poels, A. Bliek, J. Catal. 198 (2001) 77–88.

[25] E.K. Poels, J.G. Dekker, W.A. Van Leeuwen, Stud. Surf. Sci. Catal. 63 (1991) 205–214.
[26] J. Van de Loosdrecht, S. Barradas, E.A. Caricato, N.G. Ngwenya, P.S. Nkwanyana, M.A.S. Rawat, B.H. Sigwebela, P.J. Van Berge, J.L. Visagie, Top. Catal. 26 (2003) 121–127.
[27] I. Chen, S.-Y. Lin, D.-W. Shiue, Ind. Eng. Chem. Res. 27 (1988) 926.
[28] H.-C. Chen, R.B. Anderson, J. Catal. 43 (1976) 200.
[29] J.R.A. Sietsma, P.E. De Jongh, A.J. Van Dillen, K.P. De Jong, Stud. Surf. Sci. Catal. 162 (2006) 95.
[30] J.R.A. Sietsma, A.J. Van Dillen, P.E. De Jongh, K.P. De Jong, Patent application, WO2007/071899 (2005).
[31] J.R.A. Sietsma, J.D. Meeldijk, J.P. Den Breejen, M. Versluijs-Helder, A.J. Van Dillen, P.E. De Jongh, K.P. De Jong, Angew. Chem. Int. Ed. 46 (2007) 4547–4549.
[32] A.J. Koster, U. Ziese, A.J. Verkleij, A.H. Janssen, K.P. De Jong, J. Phys. Chem. B 104 (2000) 9368.
[33] A.H. Janssen, C.-M. Yang, Y. Wang, F. Schüth, A.J. Koster, K.P. De Jong, J. Phys. Chem. B 107 (2003) 10552–10556.
[34] U. Ziese, K.P. De Jong, A.J. Koster, Appl. Catal. A Gen. 260 (2004) 71.
[35] D. Zhao, J. Feng, Q. Huo, N. Melosh, G.H. Fredrickson, B.F. Chmelka, G.D. Stucky, Science 279 (1998) 548.
[36] J.R. Kremer, D.N. Mastronarde, J.R. McIntosh, J. Struct. Biol. 116 (1996) 71.
[37] M. Jaroniec, M. Kruk, J.P. Olivier, S. Koch, Stud. Surf. Sci. Catal. 128 (2000) 71–80.
[38] E.P. Barrett, L.S. Joyner, P.P. Halenda, J. Am. Chem. Soc. 73 (1951) 373.
[39] W.D. Harkins, G. Jura, J. Am. Chem. Soc. 66 (1944) 1366.
[40] M. Kruk, M. Jaroniec, A. Sayari, Langmuir 13 (1997) 6267.
[41] B.C. Lippens, J.H. De Boer, J. Catal. 4 (1965) 319–323.
[42] Sampling and analysis of commercial fats and oils method Cd 14d-99: Rapid determination of isolated trans geometric isomers (1999).
[43] Sampling and analysis of commercial fats and oils AOCS method Cc 3b-92: Slip melting point ISO standard.
[44] P. Gallezot, M. Prettre, Bull. Soc. Chim. Fr. 2 (1969) 407.
[45] J. Estellé, P. Salagre, Y. Cesteros, M. Serra, F. Medina, J.E. Sueiras, Solid State Ionics 156 (2003) 233–243.
[46] S.M. Moreno, M. Weyland, P.A. Midgley, J.F. Bengoa, M.V. Cagnoli, N.G. Gallegos, A.M. Alvarez, S.G. Marchetti, Micron 37 (2006) 52–56.
[47] M. Imperor-Clerc, D. Bazin, M.-D. Appay, P. Beaunier, A. Davidson, Chem. Mater. 16 (2004) 1813–1821.
[48] J.R.A. Sietsma, J.D. Meeldijk, M. Versluijs-Helder, A. Broersma, J. Van Dillen, P.E. De Jongh, K.P. De Jong, Chem. Mater. 20 (9) (2008) 2921–2931.
[49] H. Friedrich, J.R.A. Sietsma, P.E. De Jongh, K.P. De Jong, J. Am. Chem. Soc. 129 (2007) 10249–10254.
[50] P.I. Ravikovitch, A.V. Neimark, Langmuir 18 (2002) 9830.
[51] L. Vradman, M.V. Landau, D. Kantorovich, Y. Koltypin, A. Gedanken, Microporous Mesoporous Mater. 79 (2005) 307.
[52] P. Van Der Voort, P.I. Ravikovitch, K.P. De Jong, M. Benjelloun, E. Van Bavel, A.H. Janssen, A.V. Neimark, B.M. Weckhuysen, E.F. Vansant, J. Phys. Chem. B 106 (2006) 5873.
[53] A. Małecki, B. Małecki, Thermochim. Acta 446 (2006) 113–116.
[54] M. Maneva, N. Petroff, M. Pankova, J. Therm. Anal. 36 (1990) 577–587.
[55] X. Hou, J. Williams, K.-L. Choy, Thin Solid Films 495 (2006) 262–265.
[56] A. Roine, HSC Chemistry for Windows 4.1, Outokumpu Research Oy, Pori, Finland.
[57] A.K. Bhattacharya, J. Chem. Soc. Faraday Trans. 1 74 (1978) 1750–1757.
[58] J.C. Greaves, J.W. Linnett, Trans. Faraday Soc. 55 (1959) 1346–1354.
[59] P.G. Dickens, M.B. Sutcliffe, Trans. Faraday Soc. 60 (1964) 1272–1285.
[60] P.J. Crane, P.G. Dickens, R.E. Thomas, Trans. Faraday Soc. 63 (1967) 693–700.
[61] S.L. Soled, E. Iglesia, R.A. Fiato, J.E. Baumgartner, H. Vroman, S. Miseo, Top. Catal. 26 (2003) 101–109.
[62] J.R.A. Sietsma, A.J. Van Dillen, P.E. De Jongh, K.P. De Jong, Patent application, WO2008029177 (2008).
[63] C.J. Song, T.J. Park, S.H. Moon, Korean J. Chem. Eng. 9 (3) (1992) 159–163.
[64] G.H. Jonker, J.W. Veldsink, A.A.C.M. Beenackers, Ind. Eng. Chem. Res. 37 (1998) 4646–4656.